Honolulu, August 18–21, 2008

AIAA-2008-6603

Estimating Small-Body Gravity Field from Shape Model and Navigation Data

Ryan S. Park*, Robert A. Werner†, and Shyam Bhaskaran‡

Jet Propulsion Laboratory, California Institute of Technology, Pasadena, California, 91109

This paper presents a method to model the external gravity field and to estimate the internal density variation of a small-body. We first discuss the modeling problem, where we assume the polyhedral shape and internal density distribution are given, and model the body interior using finite elements definitions, such as cubes and spheres. The gravitational attractions computed from these approaches are compared with the true uniform-density polyhedral attraction and the level of accuracies are presented. We then discuss the inverse problem where we assume the body shape, radiometric measurements, and *a priori* density constraints are given, and estimate the internal density variation by estimating the density of each finite element. The result shows that the accuracy of the estimated density variation can be significantly improved depending on the orbit altitude, finite-element resolution, and measurement accuracy.

I. Introduction

Over the past decade, there has been a growing interest in exploring small bodies, i.e., asteroids, comets, and planetary satellites. To name a few, missions such as NEAR (1996), Deep Space 1 (1998), Stardust (1999), MUSES-C (2002), ROSETTA (2004), Deep Impact (2005), and Dawn (2007) have visited or will visit small bodies, where their mission objectives range from orbiting and flybys to landing on the surface. Among many critical requirements of such a mission, one of the most crucial components is an accurate characterization of the spacecraft orbit environment as it is usually directly related to the quality of science outcome. In general, small bodies have irregular shapes as their local gravity is not strong enough to pull the body into a concentric sphere, and thus, modeling its external gravitational field is an extremely challenging astrodynamics problem.

The first problem we discuss is the modeling problem where we assume an accurate shape model and an internal density variation of a small body is given and want to model the external gravitational field. Given an irregularly shaped body, there are basically two fundamentally different ways to model its gravitational field.[1] The first approach is to use a series expansion to approximate the gravitational potential, such as using the external spherical harmonics.[2–4] When the body in question is close to a sphere (e.g., planets) and when the field point is outside the Brillouin (i.e., circumscribing) sphere, spherical harmonics can provide a very good approximation of the overall gravitational field. When the field point is inside the Brillouin sphere, however, these series diverge in general, which makes the use of spherical harmonics not suitable especially for irregularly shaped bodies. The second approach is the direct computation of the gravitational potential using a finite number of polyhedral definitions.[5,6] This approach, however, usually assumes that the body has a constant density, and thus, it may not be a good model for a body with a strong density variation. It is possible to subdivide a polyhedron into multiple polyhedrons, but such an algorithm for subdivision is not a trivial problem.

*Member of Engineering Staff, Outer Planet Navigation Group, Jet Propulsion Laboratory, Pasadena, California, Member AAS, Member AIAA, Ryan.S.Park@jpl.nasa.gov.

†Senior Member of Engineering Staff, Optical Navigation Group, Jet Propulsion Laboratory, Pasadena, California, Robert.A.Werner@jpl.nasa.gov.

‡Group Supervisor, Outer Planet Navigation Group, Jet Propulsion Laboratory, Pasadena, California, Member AIAA, Shyam.Bhaskaran@jpl.nasa.gov.

Since we are interested in an irregularly shaped small body that has a significant density variation, the external spherical harmonics or the constant density polyhedron cannot be utilized to approximate the true gravity field. As an alternate method, we present a finite-element approach to model the gravitational potential and the necessary derivatives. We assume that a spacecraft surveys the body before the close approach, and by processing the optical data, a high-precision polyhedral shape model is available. Based on this shape model, we fill up the body interior using finite elements such as cubes (i.e., regular hexahedrons) or spheres with distinct density values. For example, Figure 1(a) is a predicted shape model of Itokawa from a radar survey prior to MUSES-C arrival and Figures 1(b) and 1(c) illustrate how a shape model can be constructed using finite cubes and spheres, respectively. Once a physical finite-element shape model is available, it is straight forward to compute the attraction whether a spacecraft is inside a Brillouin sphere or the body has a strong density variation. We compare the attraction based on finite-element shape models with the true attraction from a polyhedron model and discuss the level of accuracies.

The second problem we discuss is the inverse problem where we assume that a polyhedral body shape, radiometric measurements, and *a priori* density constraints are given, and we want to estimate the internal density variation by estimating the density of each finite element. The advantage of finite element approach is that the measurements from inside the Brillouin sphere can be utilized and estimated density has a physical meaning. In practice, this is a much more difficult problem since it is generally an ill-conditioned problem depending on the order of accuracy of the density variation one is solving for. As an example, we discuss how well the density variation can be estimated based on the polyhedral shape model shown in Figure 1(a) with different finite-element resolution, orbit altitude, and measurement accuracy.

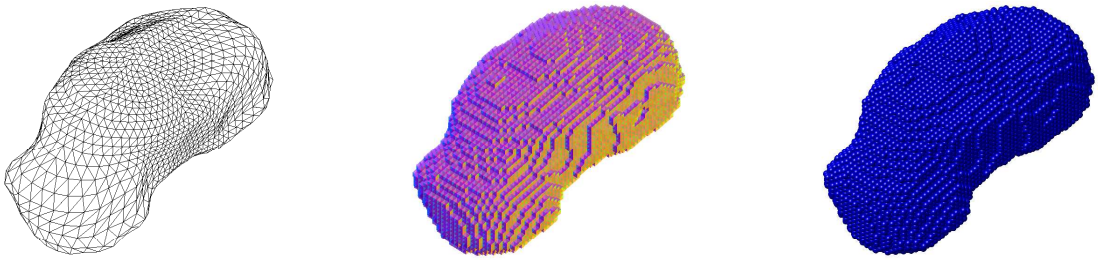

(a) Polyhedron model (3688 faces). (b) Finite-cube shape model (26311 elements). (c) Finite-sphere shape model (26311 elements).

Figure 1. Different types of a small-body shape model.

II. Gravitational Potential of a Small Body

A. Potential of a Constant-Density Polyhedron

Following the notations in Werner,[5] the gravitational potential of a polyhedral body at a field point $\mathbf{r}$ can be represented as:

$$U_p(\mathbf{r}) = \frac{1}{2}G\varrho \sum_{e\in edges} \mathbf{r}_e^T \mathbf{E}_e \mathbf{r}_e \cdot L_e - \frac{1}{2}G\varrho \sum_{f\in faces} \mathbf{r}_f^T \mathbf{F}_f \mathbf{r}_f \cdot \omega_f, \tag{1}$$

where

$$\mathbf{r}_e = \mathbf{r}_{e1} - \mathbf{r}, \tag{2}$$
$$\mathbf{E}_e = \hat{\mathbf{n}}_A(\hat{\mathbf{n}}_{12}^A)^T + \hat{\mathbf{n}}_B(\hat{\mathbf{n}}_{21}^B)^T, \tag{3}$$
$$L_e = \ln\frac{r_{e1}+r_{e2}+e_{12}}{r_{e1}+r_{e2}-e_{12}}, \tag{4}$$
$$\mathbf{r}_f = \mathbf{r}_{f1} - \mathbf{r}, \tag{5}$$
$$\mathbf{F}_f = \hat{\mathbf{n}}_f\hat{\mathbf{n}}_f^T, \tag{6}$$

$$\omega_f = \begin{cases} 2\arctan\dfrac{D_f - \mathrm{run}|\omega_\mathrm{f}|}{\overline{\mathrm{rise}|\omega_\mathrm{f}|}} & , \quad z > 0 \\ 0 & , \quad z = 0 \\ 2\arctan\dfrac{\mathrm{run}|\omega_\mathrm{f}| - \mathrm{D_f}}{-\overline{\mathrm{rise}|\omega_\mathrm{f}|}} & , \quad z < 0, \end{cases} \tag{7}$$

$$D_f = \sqrt{\left(\mathrm{run}|\omega_\mathrm{f}|\right)^2 + \left(\overline{\mathrm{rise}|\omega_\mathrm{f}|}\right)^2}, \tag{8}$$

$$\begin{bmatrix} \mathrm{run}|\omega_\mathrm{f}| \\ \overline{\mathrm{rise}|\omega_\mathrm{f}|} \end{bmatrix} = \begin{bmatrix} -\mathrm{runS_n} & \overline{\mathrm{riseS_n}} \\ -\overline{\mathrm{riseS_n}} & -\mathrm{runS_n} \end{bmatrix} \cdots \begin{bmatrix} -\mathrm{runS_2} & \overline{\mathrm{riseS_2}} \\ -\overline{\mathrm{riseS_2}} & -\mathrm{runS_2} \end{bmatrix} \begin{bmatrix} -\mathrm{runS_1} & \overline{\mathrm{riseS_1}} \\ -\overline{\mathrm{riseS_1}} & -\mathrm{runS_1} \end{bmatrix} \begin{bmatrix} 1 \\ 0 \end{bmatrix}, \tag{9}$$

$$\mathrm{runS_j} = \left(\mathbf{r}_i^T \mathbf{r}_k\right) r_j^2 - \left(\mathbf{r}_i^T \mathbf{r}_j\right) \left(\mathbf{r}_j^T \mathbf{r}_k\right), \tag{10}$$

$$\overline{\mathrm{riseS_j}} = \mathbf{r}_i \cdot (\mathbf{r}_j \times \mathbf{r}_k) \cdot r_j, \tag{11}$$

Here, G represents the universal gravitational constant, ϱ represents the body density, $\mathbf{r}_{e1}$ and $\mathbf{r}_{e2}$ represent the vectors from the field point to vertices of an edge, e_{12} represents the length of the edge, $\mathbf{r}_f$ is a vector from the field point to some fixed point in the face plane, $\hat{\mathbf{n}}_f$ is the face normal vector, $\hat{\mathbf{n}}_A$ and $\hat{\mathbf{n}}_B$ are the face normal vectors, and $\hat{\mathbf{n}}_{12}^A$ and $\hat{\mathbf{n}}_{21}^B$ are the edge normal vectors. From the potential function, the acceleration, gravity-gradient matrix, and Laplacian at a field point $\mathbf{r}$ can be derived as:

$$\frac{\partial U_p}{\partial \mathbf{r}} = -G\varrho \sum_{e \in edges} \mathbf{E}_e \mathbf{r}_e \cdot L_e + G\varrho \sum_{f \in faces} \mathbf{F}_f \mathbf{r}_f \cdot \omega_f, \tag{12}$$

$$\frac{\partial^2 U_p}{\partial \mathbf{r}^2} = G\varrho \sum_{e \in edges} \mathbf{E}_e \cdot L_e - G\varrho \sum_{f \in faces} \mathbf{F}_f \cdot \omega_f, \tag{13}$$

$$\nabla^2 U_p = -G\varrho \sum_{f \in faces} \omega_f. \tag{14}$$

Note that computing the Laplacian gives whether a field point is inside, outside, on the face, or on a vertex or an edge:

$$-\frac{\nabla^2 U_p(\mathbf{r}_i)}{G\varrho} = \begin{cases} 4\pi, & \text{if inside} \\ 0, & \text{if outside} \\ 2\pi, & \text{if on the face} \\ \text{solid angle}, & \text{if on a vertex or an edge} \end{cases}. \tag{15}$$

B. Potential of Multiple Finite-Cube and Finite-Sphere Shape Models

In order to create a finite-cube shape model from a polyhedral body, we first determine a rectangular box that circumscribes the entire body. We then mesh the rectangular box with the pre-defined cube length, ℓ, and check the Laplacian of each grid point. The grid point is stored only if it's inside the body or on the surface. This way, we obtain multiple cubes with physical length ℓ where their center points lie inside the body or on the surface. Note that this method does not perfectly model the surface variation as some cubes will have excess volumes and some polyhedron spaces will not be covered. The most trivial way to resolve this problem would be to decrease ℓ since, in the limit ($\ell \to 0$), $U_c \to U_p$, where U_c is the potential of the finite-cube shape model. This approach, however, increases the computational cost tremendously and as we will see later that estimating the density variation may become an ill-conditioned problem depending on the cube size.

Another direct way to resolve surface variation problem would be to completely cover the entire polyhedron using cubes so that there are no empty spaces left and to reshape the surface-intersecting cubes as parallelopipeds, tetrahedrons, or even general polyhedrons so that the polyhedron surface can be approximated more accurately. An indirect, yet simpler, way would be to apply density that is proportional to the volume difference to the surface-intersecting cubes.[a] These approaches would yield physically more accurate shape representations, but are not considered in this study.

[a]This density correction method can also be applied to a finite-sphere shape model as well.

Given multiple cubes, it is straight forward to come up with the following gravitational potential function and related derivatives at a field point $\mathbf{r}$:

$$U_c(\mathbf{r}) = \sum_{i\in cubes}\left(\frac{1}{2}G\varrho_i\sum_{e\in edges}\mathbf{r}_e^T\mathbf{E}_e\mathbf{r}_e\cdot L_e - \frac{1}{2}G\varrho_i\sum_{f\in faces}\mathbf{r}_f^T\mathbf{F}_f\mathbf{r}_f\cdot\omega_f\right), \tag{16}$$

$$\frac{\partial U_c}{\partial\mathbf{r}} = \sum_{i\in cubes}\left(-G\varrho_i\sum_{e\in edges}\mathbf{E}_e\mathbf{r}_e\cdot L_e + G\varrho_i\sum_{f\in faces}\mathbf{F}_f\mathbf{r}_f\cdot\omega_f\right), \tag{17}$$

$$\frac{\partial^2 U_c}{\partial\mathbf{r}^2} = \sum_{i\in cubes}\left(G\varrho_i\sum_{e\in edges}\mathbf{E}_e\cdot L_e - G\varrho_i\sum_{f\in faces}\mathbf{F}_f\cdot\omega_f\right), \tag{18}$$

$$\frac{\partial}{\partial\varrho_j}\left(\frac{\partial U_c}{\partial\mathbf{r}}\right) = \sum_{i\in cubes}\left(-G\delta_{ij}\sum_{e\in edges}\mathbf{E}_e\mathbf{r}_e\cdot L_e + G\delta_{ij}\sum_{f\in faces}\mathbf{F}_f\mathbf{r}_f\cdot\omega_f\right), \tag{19}$$

where δ_{ij} represents the Kronecker delta function.

If we model the shape using spheres (i.e., point masses), the corresponding gravitational potential, acceleration, gravity-gradient matrix, and partial of acceleration with respect to density are:

$$U_m(\mathbf{r}) = \sum_{i\in spheres}\frac{4\pi}{3}r_{mi}^3G\varrho_i\frac{1}{||\mathbf{r}-\mathbf{r}_i||}, \tag{20}$$

$$\frac{\partial U_m}{\partial\mathbf{r}} = \sum_{i\in spheres}-\frac{4\pi}{3}r_{mi}^3G\varrho_i\frac{\mathbf{r}-\mathbf{r}_i}{||\mathbf{r}-\mathbf{r}_i||^3}, \tag{21}$$

$$\frac{\partial^2 U_m}{\partial\mathbf{r}^2} = \sum_{i\in spheres}\frac{4\pi}{3}r_{mi}^3G\varrho_i\frac{1}{||\mathbf{r}-\mathbf{r}_i||^5}\left[\mathbf{I}_{3\times3}-3\frac{(\mathbf{r}-\mathbf{r}_i)(\mathbf{r}-\mathbf{r}_i)^T}{||\mathbf{r}-\mathbf{r}_i||^2}\right], \tag{22}$$

$$\frac{\partial}{\partial\varrho_j}\left(\frac{\partial U_m}{\partial\mathbf{r}}\right) = -\frac{4\pi}{3}r_{mj}^3G\frac{\mathbf{r}-\mathbf{r}_j}{||\mathbf{r}-\mathbf{r}_j||^3}, \tag{23}$$

where $\mathbf{r}_i$ and r_{mi} represent the position vector and the radius of an i^{th} sphere. Note that a finite cube can always be modeled using finite spheres since we can always reduce the size of spheres to fill up the cube. This approach, as discussed earlier in this section, would increase the computational cost and estimating the density variation may become an ill-conditioned problem.

C. Comparison of the Attractions of a Finite Cube and a Finite Sphere

Consider a cube with a length ℓ. Assuming a sphere has the same density and mass as the cube, its corresponding radius is $r_m = (3/4\pi)^{1/3}\ell \approx 0.62\ell$. We want the masses to be the same because the point-mass approximations of both shapes should be identical.

Now define λ_{ij} as follows:

$$\lambda_{ij} = \frac{\|\partial U_i/\partial\mathbf{r} - \partial U_j/\partial\mathbf{r}\|}{\|\partial U_i/\partial\mathbf{r}\|}\times 100\ \%, \tag{24}$$

which represents the percent difference between the attractions from the model i and model j, e.g., λ_{cm} represents the percent difference between finite-cube and finite-sphere shape models. Assuming a unit cube, Figure 2 shows λ_{cm} along x-y plane, which is also discussed in the work of Werner and Scheeres.[6] Since the masses are the same, we know that, in the limit ($||\mathbf{r}|| \to \infty$), $\lambda_{cm} \to 0$ %. We note that, in general, the difference is very small ($\lambda_{cm} < 0.5$ %) when the field point is about 2ℓ distance away from the center. The maximums occur on the surfaces ($\lambda_{cm} \approx 54$ %). This indicates that, depending on the location of the field point, a cube can be approximated as a sphere, which is generally easier to implement and computationally faster.

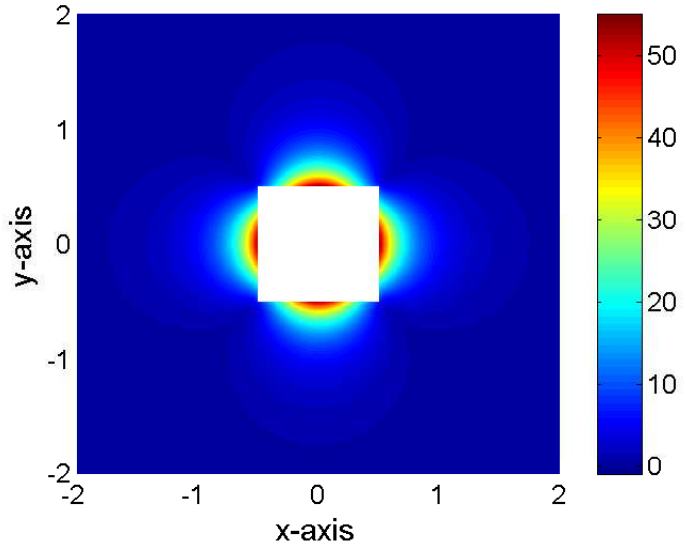

Figure 2. Percent difference between the attractions from a finite cube and a finite sphere.

D. Comparison of the Attractions of Finite-Cube, Finite-Sphere, and Polyhedral Shape Models

Consider the tetrahedral Itokawa polyhedral shape model shown in Figure 1(a), which has 1846 vertices and 3688 faces. In this study, the polyhedron density is assumed to be constant[7] (1.9 g/cm^3) and the volume is computed to be[8] $\sum_{i \in faces} \det\left[\mathbf{r}_{i1},\ \mathbf{r}_{i2},\ \mathbf{r}_{i3}\right]/6 = 0.026278$ km^3, where $\mathbf{r}_{ij}$ is the j^{th} vertex position vector of the i^{th} face.

We model the polyhedral shape using finite elements based on the method discussed in Section II.B. Assuming a 20 m resolution finite-cube shape model, there are 3292 cubes, and in order to keep total mass the same, the density of each cube is corrected to $M_{\text{Itokawa}}/V_{\text{total cubes}} = 1.896$ g/cm^3, where $V_{\text{total cubes}} = 0.026336$ km^3. The finite-sphere shape model is obtained in a similar manner where each sphere has the corresponding radius of 12.41 m.[b]

Figures 3(a-c) show the attractions, i.e., $\partial U_c/\partial \mathbf{r}$, based on a finite-cube shape model along different cross-sections. As expected, we observe irregular gravitational attractions near the surface and becomes more concentrically distributed as the field point moves away from the center. Figures 4(a,c,e) show λ_{pc}, which represents the percent difference in the attractions between the polyhedral and finite-cube shape models. We observe a poor agreement near the surface, which is mostly because the surface variation is not modeled as discussed in Section II.B. Figures 4(b,d,f) show λ_{cm}, and as expected, we observe a very good agreement except for the points near the surface, which is essentially the result discussed in Section II.C.

[b]Each cube and sphere are assumed to have the same density, mass, and volume, and thus, the only difference is their physical shapes.

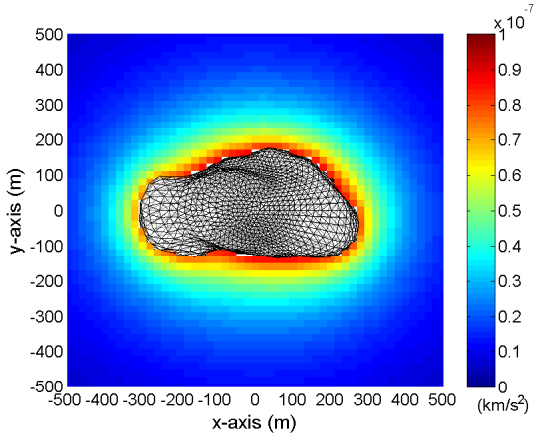

(a) Along x-y plane.

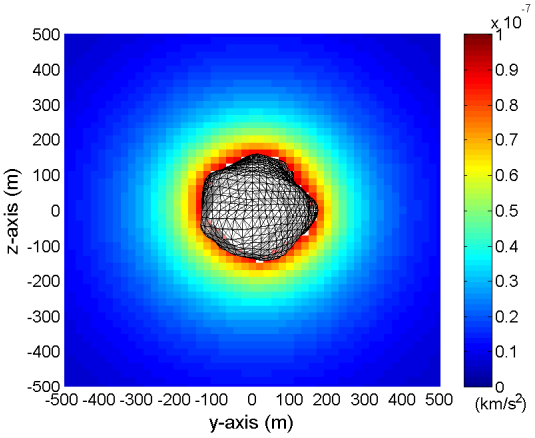

(b) Along y-z plane.

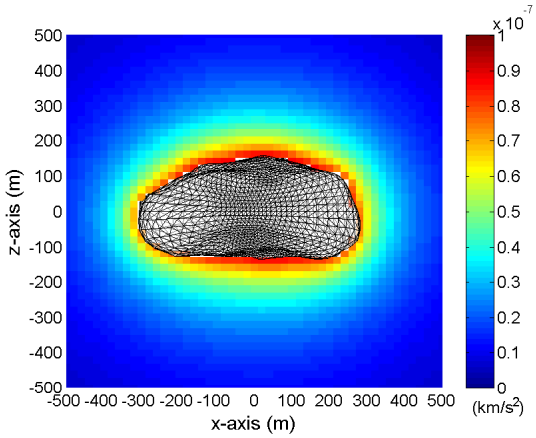

(c) Along x-z plane.

Figure 3. Attraction of the finite-cube shape model.

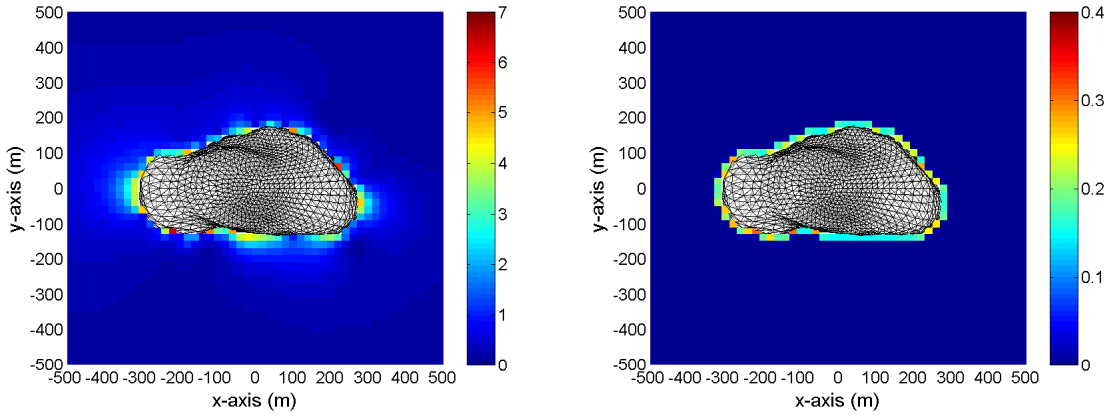

(a) Along x-y plane (λ_{pc}).

(b) Along x-y plane (λ_{cm}).

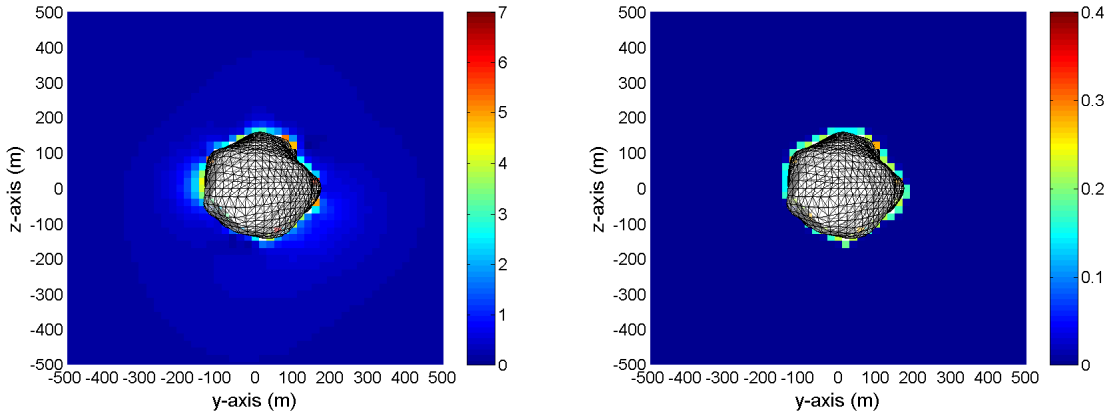

(c) Along y-z plane (λ_{pc}).

(d) Along y-z plane (λ_{cm}).

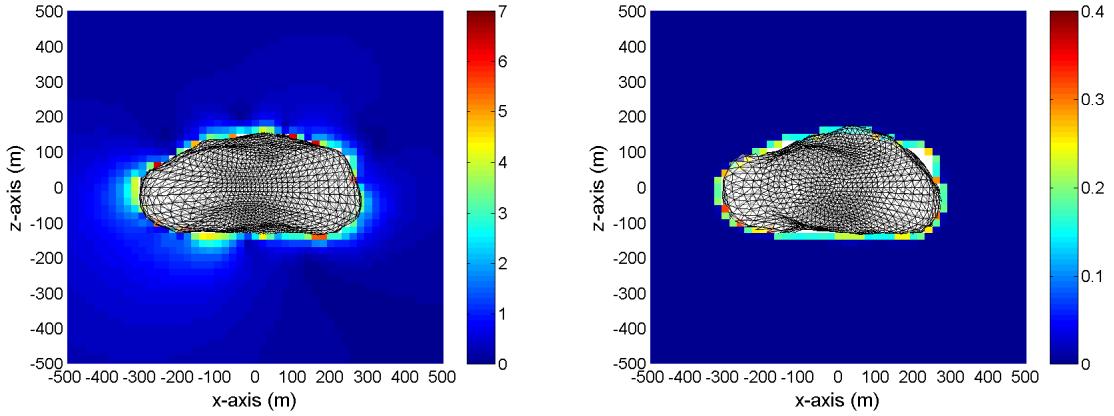

(e) Along x-z plane (λ_{pc}).

(f) Along x-z plane (λ_{cm}).

Figure 4. Comparison of the attractions from polyhedral, finite-cube (20 m length), and finite-sphere (12.41 m radius) shape models. The figures on the left show λ_{pc} and the figures on the a right show λ_{cm} along different cross-sections.

III. Covariance Analysis

A. Batch Least-Squares Filter

Define the cost function J as follows:

$$J(\mathbf{x}_0) \;=\; \frac{1}{2}\left(\mathbf{x}_0-\mathbf{x}_a\right)^T\mathbf{\Lambda}_a\left(\mathbf{x}_0-\mathbf{x}_a\right)+\frac{1}{2}\left[\mathbf{z}^*-\mathbf{z}(\mathbf{x}_0)\right]^T\mathbf{W}\left[\mathbf{z}^*-\mathbf{z}(\mathbf{x}_0)\right], \tag{25}$$

where $\mathbf{x}_a$ is the *a priori* state estimate, $\mathbf{\Lambda}_a$ is the *a priori* information matrix, $\mathbf{z}^*$ is the actual measurement vector (i.e., observed data), $\mathbf{z}$ is the predicted measurement vector, $\mathbf{W}$ is the measurement weight matrix, and $\mathbf{x}_0$ is the estimated initial state vector.[c] Under ideal conditions, i.e., perfect dynamical model and observables, the cost function J should vanish to zero for each $\mathbf{x}_0$. In practice, however, there always exist errors in both the dynamics and measurement models. The goal of the batch least-squares filter is to find the initial state $\mathbf{x}_0$ such that the cost function J is minimized given $\mathbf{z}^*$.

By applying the necessary conditions to Eqn. (25) and by linearizing about the nominal trajectory, $\bar{\mathbf{x}}_0$, the following normal equation is obtained:[9,10]

$$\begin{aligned}\underbrace{\left[\mathbf{\Lambda}_a+\mathbf{H}_{\mathbf{x}_0}^T\mathbf{W}\mathbf{H}_{\mathbf{x}_0}\right]}_{\mathbf{\Lambda}_0}\delta\mathbf{x}_0 \;&=\; \underbrace{\mathbf{\Lambda}_a\delta\mathbf{x}_a+\mathbf{H}_{\mathbf{x}_0}^T\mathbf{W}\Delta\mathbf{z}}_{\tilde{\mathbf{z}}},\\ \mathbf{\Lambda}_0\,\delta\mathbf{x}_0 \;&=\; \tilde{\mathbf{z}},\end{aligned} \tag{26}$$

where $\delta\mathbf{x}_a=\mathbf{x}_a-\bar{\mathbf{x}}_0$, $\Delta\mathbf{z}=\mathbf{z}^*-\mathbf{z}(\bar{\mathbf{x}}_0)$, and

$$\mathbf{H}_{\mathbf{x}_0} \;=\; \left.\frac{\partial\mathbf{z}}{\partial\mathbf{x}_0}\right|_{\mathbf{x}_0=\bar{\mathbf{x}}_0} \;=\; \begin{bmatrix}\mathbf{h}_1\mathbf{\Phi}_1\\ \vdots\\ \mathbf{h}_N\mathbf{\Phi}_N\end{bmatrix}. \tag{27}$$

Here, $\mathbf{\Lambda}_0$ is called the epoch-state information matrix, $\tilde{\mathbf{z}}$ is called the data vector, and $\mathbf{\Phi}_k=\mathbf{\Phi}(t_k,t_0)$ is the usual state transition matrix (STM) mapping the deviation from t_0 to t_k, i.e.,

$$\dot{\mathbf{\Phi}} \;=\; \frac{\partial}{\partial\mathbf{x}}\left(\frac{d\mathbf{x}}{dt}\right)\mathbf{\Phi} \;=\; \mathbf{A}\mathbf{\Phi}. \tag{28}$$

In summation notation, the epoch-state information matrix and the data vector can then be stated as:

$$\mathbf{\Lambda}_0 \;=\; \mathbf{\Lambda}_a+\sum_{k=1}^{N}\frac{1}{\sigma_k^2}\mathbf{\Phi}_k^T\mathbf{h}_k^T\mathbf{h}_k\mathbf{\Phi}_k, \tag{29}$$

$$\tilde{\mathbf{z}} \;=\; \mathbf{\Lambda}_a\delta\mathbf{x}_a+\sum_{k=1}^{N}\frac{1}{\sigma_k^2}\mathbf{\Phi}_k^T\mathbf{h}_k^T[z_k^*-z_k(\bar{\mathbf{x}}_0)]. \tag{30}$$

The least squares filter computes the correction vector $\delta\mathbf{x}_0$ and iterates until the solution converges, which usually depends on some user-defined quantities, e.g., $||\delta\mathbf{x}_0||<\epsilon_{\delta\mathbf{x}_0}$. When carrying out a *batch least-squares covariance analysis*, however, one is only interested in computing $\mathbf{\Lambda}_0$ as it conveys how well the estimations of the estimate vector $\mathbf{x}_0$ can be made by processing N measurements. To see this, let each measurement have Gaussian statistics so that each residual can be represented as $\boldsymbol{\epsilon}=\mathbf{z}^*-\mathbf{z}(\mathbf{x}_0)\sim\mathcal{N}(\mathbf{0},\mathbf{\Sigma})$, which is a usual assumption made in conventional trajectory navigation. Given the statistical properties of the processed measurements, we want to characterize the statistics of the estimate vector $\mathbf{x}_0$. Computing the first two central moments results in, i.e., conditional mean and covariance matrix:

$$\mathrm{E}[\mathbf{x}_0^{\mathrm{lsq}}] \;=\; \mathrm{E}\left[\bar{\mathbf{x}}_0+\delta\mathbf{x}_0\right] \;=\; \mathbf{x}_0, \tag{31}$$

$$\mathbf{P}_0^{\mathrm{lsq}} \;=\; \mathrm{E}\left[(\mathbf{x}_0^{\mathrm{lsq}}-\mathrm{E}[\mathbf{x}_0^{\mathrm{lsq}}])(\mathbf{x}_0^{\mathrm{lsq}}-\mathrm{E}[\mathbf{x}_0^{\mathrm{lsq}}])^T\right] \;=\; \left(\mathbf{\Lambda}_a+\mathbf{H}_{\mathbf{x}_0}^T\mathbf{W}\mathbf{H}_{\mathbf{x}_0}\right)^{-1}. \tag{32}$$

[c] Note that $\mathbf{x}_0$ is not necessarily limited to the spacecraft initial state vector. It can be augmented to include any parameters of interest, such as dynamics and measurement biases.

Therefore, we can conclude that the estimate vector $\mathbf{x}_0$ is indeed a Gaussian vector with $\mathbf{x}_0^{\text{lsq}} \sim \mathcal{N}(\mathbf{x}_0, \mathbf{\Lambda}_0^{-1})$, or the full Gaussian probability density function of $\mathbf{x}_0^{\text{lsq}}$ can be given as:

$$p(\mathbf{x}_0^{\text{lsq}}) = \frac{\sqrt{\det \mathbf{\Lambda}_0}}{(2\pi)^{n/2}} \exp\left[-\frac{1}{2}(\mathbf{x}_0^{\text{lsq}} - \mathbf{x}_0)^T \mathbf{\Lambda}_0 (\mathbf{x}_0^{\text{lsq}} - \mathbf{x}_0)\right], \tag{33}$$

$$\Pr(\mathbf{x}_0^{\text{lsq}} \in \mathcal{B}) = \int_{\mathcal{B}} p(\mathbf{x}_0)\, d\mathbf{x}_0. \tag{34}$$

Therefore, it is evident that the information matrix $\mathbf{\Lambda}_0$ characterizes the statistical properties of $\mathbf{x}_0$, and thus, the least-squares covariance analysis is a useful filter design tool. In this paper, we carry out a batch least-squares covariance analysis rather than a full estimation simulation since our goal is to analyze the level of expected accuracies of the estimated densities from processing radiometric measurements.

B. Square-Root Information Filter Measurement Update

It has been known for many years that numerical precision is often lost in the covariance computation due to numerical round-off and measurement update (i.e., matrix inversion) errors. A method for retaining precision is to use the square-root information filter (SRIF):[9,11]

$$\mathbf{\Lambda}_0 = \mathbf{R}_0^T \mathbf{R}_0, \tag{35}$$

where $\mathbf{R}_0$ is the epoch-state SRIF matrix which we update at every measurement increment. When a measurement is updated at t_k:

$$\mathbf{\Lambda}_0^+ = \mathbf{R}_0^T \mathbf{R}_0 + \frac{1}{\sigma_k^2} \mathbf{\Phi}_k^T \mathbf{h}_k^T \mathbf{h}_k \mathbf{\Phi}_k = \begin{bmatrix} \mathbf{R}_0 \\ \dfrac{\mathbf{h}_k \mathbf{\Phi}_k}{\sigma_k} \end{bmatrix}^T \mathbf{T}_H^T \mathbf{T}_H \begin{bmatrix} \mathbf{R}_0 \\ \dfrac{\mathbf{h}_k \mathbf{\Phi}_k}{\sigma_k} \end{bmatrix} = \begin{bmatrix} \mathbf{R}_H \\ \mathbf{0} \end{bmatrix}^T \begin{bmatrix} \mathbf{R}_H \\ \mathbf{0} \end{bmatrix}, \tag{36}$$

where $\mathbf{T}_H$ is an orthogonal Householder transformation matrix which satisfies $\mathbf{T}_H^T \mathbf{T}_H = \mathbf{I}$ and $\mathbf{R}_H$ is an upper triangular matrix which becomes the updated epoch-state SRIF matrix. In the actual computation, we adopt QR-factorization as the Householder transformation.[12] After the Householder transformation is applied, the updated epoch-state information matrix becomes:

$$\mathbf{\Lambda}_0^+ = \mathbf{R}_H^T \mathbf{R}_H, \tag{37}$$

and the updated epoch-state covariance matrix yields:

$$\mathbf{P}_0^+ = \mathbf{R}_H^{-1} \mathbf{R}_H^{-T}, \tag{38}$$

which represents the *a posteriori* uncertainty of the estimated initial state vector.

IV. Estimation of the Small-Body Density Distribution

A. Correlation between Two Finite Spheres

Before carrying out a full covariance analysis, we would like to understand how well we can decouple the information content from a single measurement when estimating the density of multiple finite elements. Consider two finite spheres located at $\mp\mathbf{c} = [\mp c,\ 0,\ 0]$ with volumes V_1 and V_2 and densities ϱ_1 and ϱ_2. The total attraction from two finite spheres is then:

$$\mathbf{a} = -G\left(\varrho_1 V_1 \frac{\mathbf{r}+\mathbf{c}}{||\mathbf{r}+\mathbf{c}||^3} + \varrho_2 V_2 \frac{\mathbf{r}-\mathbf{c}}{||\mathbf{r}-\mathbf{c}||^3}\right). \tag{39}$$

Now suppose we can directly measure the acceleration and compute the measurement partials, i.e.,

$$\mathbf{h} = \left[\ -V_1 G\left(\frac{\mathbf{r}+\mathbf{c}}{||\mathbf{r}+\mathbf{c}||^3}\right),\quad -V_2 G\left(\frac{\mathbf{r}-\mathbf{c}}{||\mathbf{r}-\mathbf{c}||^3}\right)\ \right]. \tag{40}$$

The epoch-state information matrix can be computed as $\mathbf{\Lambda}_0 = \mathbf{h}^T\mathbf{h}$, so that $\mathbf{P}_0 = \mathbf{\Lambda}_0^{-1}$. Figure 5 shows the correlation coefficient between finite-sphere densities, i.e., $\mathbf{P}_{0,12}/\sqrt{\mathbf{P}_{0,11}\mathbf{P}_{0,22}}$, and note that both x and y axes are normalized by the radius c.[d] We are interested in the correlation coefficient because it is the measure of how much information content of a single acceleration measurement can be used to decouple the estimates of ϱ_1 and ϱ_2. Note that the correlation coefficient is invariant under the volume and density of finite spheres since only one measurement is taken at time zero. The result shows that the field point has to be at a close distance in order to obtain a meaningful measurement. Also, note that the information matrix is not invertible along the points $y = 0$, which is expected as the acceleration directions due to each finite sphere are parallel. The zero correlation occur when the field point to finite-sphere vectors are perpendicular, i.e., the circle at the origin with radius c.

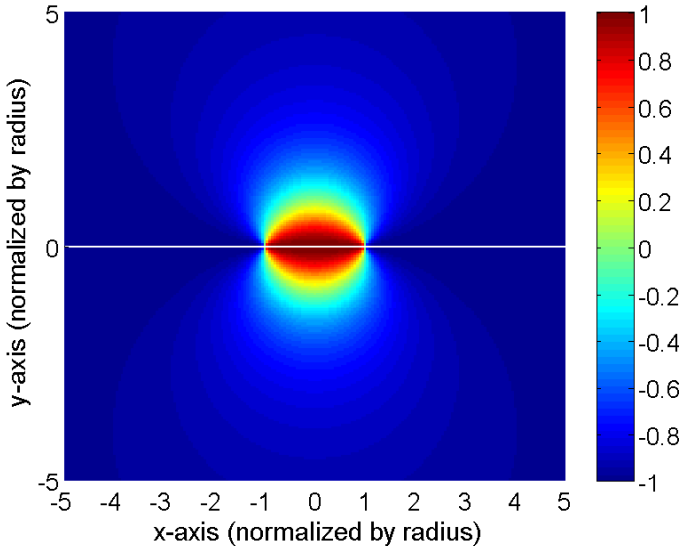

Figure 5. Correlation of the estimated densities of two finite spheres.

B. Estimated Uncertainties of Finite-Cube and Finite-Sphere Shape Models

In the full covariance analysis, the estimated variables are the initial spacecraft state and the density of each finite element, i.e.,

$$\mathbf{x} = \left[\mathbf{r}_0^T, \quad \mathbf{v}_0^T, \quad \mathbf{p}^T \right]^T, \tag{41}$$

where

$$\mathbf{p} = \left[\varrho_1, \quad \cdots, \quad \varrho_M \right]^T. \tag{42}$$

Note that ϱ_j is the density of the j^{th} element where $j \in \{1, \cdots, M\}$ depends on the number of elements in the finite-element shape model. The equations of motion for the estimated vector are:

$$\dot{\mathbf{x}} = \left[\mathbf{v}^T, \quad \frac{\partial U_i}{\partial \mathbf{r}}, \quad \mathbf{0}_{1\times M} \right]^T, \tag{43}$$

and the corresponding differential equations for the STM yields:

$$\dot{\mathbf{\Phi}} = \begin{bmatrix} \mathbf{0}_{3\times 3} & \mathbf{I}_{3\times 3} & \mathbf{0}_{3\times M} \\ \dfrac{\partial^2 U_i}{\partial \mathbf{r}^2} & \mathbf{0}_{3\times 3} & \dfrac{\partial}{\partial \mathbf{p}}\left(\dfrac{\partial U_i}{\partial \mathbf{r}}\right) \\ \mathbf{0}_{M\times 3} & \mathbf{0}_{M\times 3} & \mathbf{0}_{M\times M} \end{bmatrix} \mathbf{\Phi}, \tag{44}$$

[d]The x and y axes are normalized by the radius (c) so that two finite spheres are located at (-1,0) and (1,0).

where $i \in \{c, m\}$ for either a finite-cube or a finite-sphere shape model. In the actual computation, the integration of the STM of **p** is excluded since it's always an $M \times M$ identity matrix. Note that, at each point of integration, the Jacobi constant ($\mathcal{J}$) is computed as a validation check,[e] i.e.,

$$\mathcal{J} \;=\; \frac{1}{2}\left(\dot{x}^2 + \dot{y}^2 + \dot{z}^2\right) - U_i(x, y, z). \tag{45}$$

Our goal is to analyze how well we can estimate the density vector **p** based on radiometric measurements. In this study, the first data type we consider is instantaneous range measurements:[f]

$$z_R \;=\; ||\mathbf{r} - \mathbf{r}_s|| \;=\; ||\boldsymbol{\rho}|| \;=\; \rho, \tag{46}$$

where $\mathbf{r}_s$ is the station location vector. Taking the partials of the range measurement with respect to the current state vector **x** yields:[11,13]

$$\mathbf{h}_R \;=\; \frac{\partial z_R}{\partial \mathbf{x}} \;=\; \left[\; \frac{\partial z_R}{\partial \mathbf{r}},\;\; \frac{\partial z_R}{\partial \mathbf{v}},\;\; \frac{\partial z_R}{\partial \mathbf{p}} \;\right] \;=\; \left[\; \hat{\boldsymbol{\rho}}^T,\;\; \mathbf{0}_{1\times 3},\;\; \mathbf{0}_{1\times M} \;\right], \tag{47}$$

where $\hat{\boldsymbol{\rho}}$ is the unit tracking station to spacecraft position vector.

The second data type we consider are instantaneous range-rate measurements.[g] Its analytic representation is:

$$z_D \;=\; \frac{d}{dt}||\mathbf{r} - \mathbf{r}_s|| \;=\; \hat{\boldsymbol{\rho}} \cdot \dot{\boldsymbol{\rho}}. \tag{48}$$

Taking partials gives:

$$\mathbf{h}_D \;=\; \frac{\partial z_D}{\partial \mathbf{x}} \;=\; \left[\; \dot{\boldsymbol{\rho}}^T \left(\frac{\partial \hat{\boldsymbol{\rho}}}{\partial \mathbf{r}}\right)^T,\;\; \hat{\boldsymbol{\rho}}^T,\;\; \mathbf{0}_{1\times M} \;\right], \tag{49}$$

where

$$\frac{\partial \hat{\boldsymbol{\rho}}}{\partial \mathbf{r}} \;=\; \frac{1}{\rho}\left[\mathbf{I}_{3\times 3} - \hat{\boldsymbol{\rho}}\hat{\boldsymbol{\rho}}^T\right]. \tag{50}$$

Throughout this paper, the following assumptions are made:

1. The central body is non-rotating.
2. One tracking station is located at 2.5 km along the $+y$ axis.
3. The small-body occultation effect is ignored.
4. All trajectories are integrated for 5 days.
5. Both range and range-rate measurements are taken every 15 minutes.
6. Assuming X-band capability, the measurement accuracies are assumed to be 5 m and 0.075 mm/s for range and range-rate data, respectively.
7. The *a priori* covariance matrix is assumed to be diagonal with (50 m)^2, (0.01 m/s)^2, and (50% of the given density)^2 (i.e., 0.946 g/m^3 for 50 m or 0.948 g/m^3 for 20 m finite cubes) for position, velocity, and density components, respectively.

Table 1: Initial states used in covariance analysis simulation.

	Initial Position (m)	Initial Velocity (m/s)	Initial Orbit Period (hours)
Case 1	$\mathbf{r}_0 = [\,-360,\ 0,\ 0]^T$	$\mathbf{v}_0 = [\,0, -0.12026, 0]^T$	22.6
Case 2	$\mathbf{r}_0 = [\,0,\ 200,\ 0]^T$	$\mathbf{v}_0 = [\,0.05,\ 0,\ 0.1188]^T$	2.69

[e] Since the gravity is a conservative force (i.e., energy is conserved) the Jacobi constant must be constant at all times.

[f] In practice, the instantaneous range measurements are modeled as the uplink and downlink signal travel times.

[g] The information content of an instantaneous range-rate measurement is essentially the Doppler frequency shift in the transmitted signals.

Figures 6(a) and 7(a) show the *Case 1* initial state integrated based on 50 m resolution finite-cube and finite-sphere shape models, where the grid points are generated from the Itokawa shape model (i.e., Figure 1(a)) using the method discussed in Section II.B. There are total of 211 elements, the nominal density of 1.9 g/m^3 is corrected to 1.893 g/m^3 to retain the same mass, and the corresponding finite-sphere radius is 31.02 m. Figure 6(b) shows the *a posteriori* density uncertainties along cross-sections defined by constant z-planes of the shape model shown in Figure 6(a), where the green arrow represents the $+z$ axis. Recall that the *a priori* density uncertainties are 50 % for each element. As expected, only the cubes near the surface, where close flybys occur, have significant uncertainty improvement. The estimated root-sum-square (RSS) of the *a posteriori* position uncertainties were $\approx$ 1 m and 0.25 mm/s for position and velocity, respectively. Figure 7(b) shows the same case based on a finite-sphere shape model and we observe the same behavior as shown in Figure 6(b).

Figure 8(a) shows the *Case 1* initial state integrated based on a 20 m resolution finite-cube shape model, which corresponds to 3292 finite cubes. In this case, the nominal density is corrected to 1.896 g/m^3. Figure 8(b) shows the estimated *a posteriori* density uncertainties of each 20 m resolution finite cube and we observe almost negligible change in the density uncertainties when compared to the 50% *a priori* density uncertainty. This is mainly because the flyby distance is not close enough to decouple the measurement information content for each finite cube. This behavior is similar fundamental limit which exists when estimating the spherical harmonics from a spacecraft trajectory. Depending on the orbit altitude, there exists a limit on up to what degree and order spherical harmonic coefficients can be estimated.[14]

Figures 9(a) and 10(a) show the *Case 2* initial state integrated based on 50 m resolution finite-cube and finite-sphere shape models, respectively. Figure 9(b) shows the estimated uncertainties along the constant z planes. We observe improved uncertainty accuracies which is mainly due to decreased orbit altitude. Although it's not shown here, modeling the body shape using finite spheres yields essentially the same result. Figure 10(b) shows the same case based on the corresponding finite-sphere shape model and more accurate measurement accuracies of 0.5 m and 0.0075 mm/s for range and range-rate, respectively. When compared to Figure 9(b), we observe significant improvement, where the improvement ranges from factor of 1 to 6.2. A similar result is obtained when we model the body shape using finite-cubes.

V. Conclusion

In this study, we have presented a finite-element based approach to model the external gravitational field and to estimate the internal density variation of a small body. Given a polyhedral shape model, the body interior was filled using finite elements, such as cubes and spheres, and we showed that, depending on the finite-element resolution and field-point distance from the small body, the finite-element approach provides a very good approximation of the polyhedral gravity field. The main error comes from neglecting the surface variation and we discussed potential ways to resolve this problem. Also, finite-cube and finite-sphere shape models showed noticeable difference only when the field point is very close to the surface.

We also presented the covariance analysis of an inverse problem where a shape model, radiometric measurements, and *a priori* density constraints are given, and we attempt to solve for the internal density variation by estimating the density of each finite element. In practice, we will probably need to apply a bootstrap method where we start from large finite elements and refine as the the orbit altitude is lowered. Another potential approach would be to estimate the spherical harmonics when the spacecraft is outside of the Brillouin sphere, and solve for the initial guess of the internal density values using a method such as discussed by Scheeres *et al.*.[15] As a result, we have shown that the accuracy of the estimated density uncertainties can be significantly improved depending on the finite-element resolution, orbit altitude, and radiometric measurement accuracy.

VI. Acknowledgement

The research described in this paper was carried out at the Jet Propulsion Laboratory, California Institute of Technology, under a contract with the National Aeronautics and Space Administration. The authors would like to thank Dr. A. Konopliv, Dr. T.H. Sweetser, and Dr. D.-N. Yuan from the Jet Propulsion Laboratory for their helpful comments and suggestions.

References

[1]Casotto, S. and Musotto, S., "Methods for Computing the Potential of an Irregular, Homogeneous, Solid Body and its Gradient," *Astrodynamics Specialist Conference*, 2000, AIAA-2000-4023.

[2]Kaula, W., *Theory of Satellite Geodesy Applications of Satellites to Geodesy*, Dover Publications, 2000.

[3]Roy, A., *Orbital Motion*, Institute of Physics Publishing, third edition, reprinted ed., 1998.

[4]Garmier, R. and Barriot, J.-P., "Ellipsoidal Harmonic Expressions of the Gravitational Potential: Theory and Applications," *Celestial Mechanics and Dynamical Astronomy*, Vol. 79, 2001, pp. 235–275.

[5]Werner, R., *On the Gravity Field of Irregularly Shaped Celestial Bodies*, Ph.D. thesis, The University of Texas at Austin, 1996.

[6]Werner, R. and Scheeres, D., "Exterior Gravitation of a Polyhedron Derived and Compared with Harmonic and Mascon Gravitation Representations of Asteroid 4769 Castalia," *Celestial Mechanics and Dynamical Astronomy*, Vol. 65, 1997, pp. 313–344.

[7]Fujiwara, A., Kawaguchi, J., Yeomans, D. K., Abe, M., Mukai, T., Okada, T., Saito, J., Yano, H., Yoshikawa, M., Scheeres, D. J., Barnouin-Jha, O., Cheng, A. F., Demura, H., Gaskell, R. W., Hirata, N., Ikeda, H., Kominato, T., Miyamoto, H., Nakamura, A. M., Nakamura, R., Sasaki, S., and Uesugi, K., "The Rubble-Pile Asteroid Itokawa as Observed by Hayabusa," *Science*, Vol. 312, 2006, pp. 1330–1334.

[8]Werner, R., "Spherical Harmonic Coefficients for the Potential of a Constant-Density Polyhedron," *Computers & Geosciences*, Vol. 23, No. 10, 1997, pp. 1071–1077.

[9]Bierman, G., *Factorization Methods for Discrete Sequential Estimation*, Vol. 128, Academic Press, 1977.

[10]Crassidis, J. and Junkins, J., *Optimal Estimation of Dynamics Systems*, CRC Press LLC, 2004.

[11]Park, R., Scheeres, D., Giampieri, G., Longuski, J., and Fischbach, E., "A Test of General Relativity: Estimating the Parameterized Post-Newtonian Parameters from Spacecraft Radiometric Measurements," *Journal of Spacecraft and Rockets*, Vol. 42, No. 3, 2005, pp. 559–568.

[12]Montenbruck, O. and Gill, E., *Satellite Orbits*, Springer, 2nd ed., 2001.

[13]Longuski, J., Fischbach, E., Scheeres, D., Giampieri, G., and Park, R., "Deflection of Spacecraft Trajectories as a New Test of General Relativity: Determining the PPN Parameters β and γ," *Phys. Rev. D*, Vol. 69, No. 042001, 2004, pp. 042001–1–042001–15.

[14]Konopliv, A., Miller, J., Owen, W., Yeomans, D., Giorgini, J., Garmier, R., and Barriot, J.-P., "A Global Solution for the Gravity Field, Rotation, Landmarks, and Ephemeris of Eros," *Icarus*, Vol. 160, 2002, pp. 289–299.

[15]Scheeres, D., Khushalani, B., and Werner, R., "Estimating Asteroid Density Distributions from Shape and Gravity Information," *Planetary and Space Science*, Vol. 48, 2000, pp. 965–971.

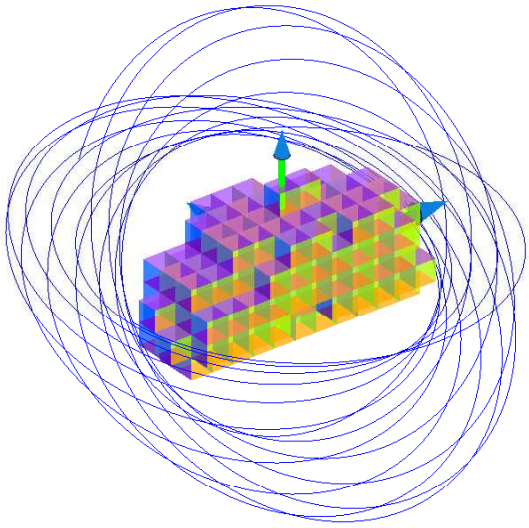

(a) 3-d trajectory and finite-cube shape model (211 elements).

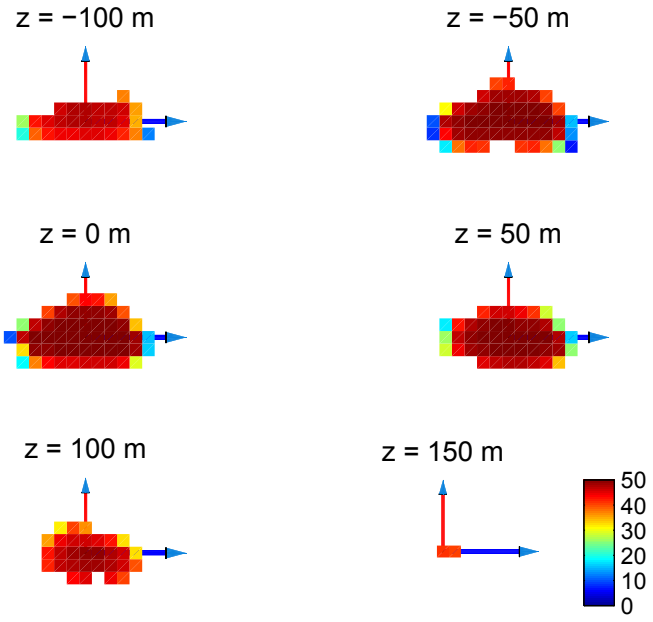

(b) Density uncertainties along the x-y plane (%).

Figure 6. *Case 1* trajectory based on 50 m cube resolution.

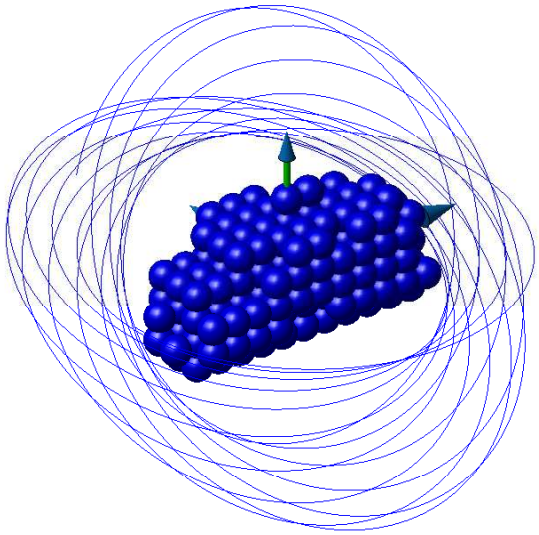

(a) 3-d trajectory and finite-sphere shape model (211 elements).

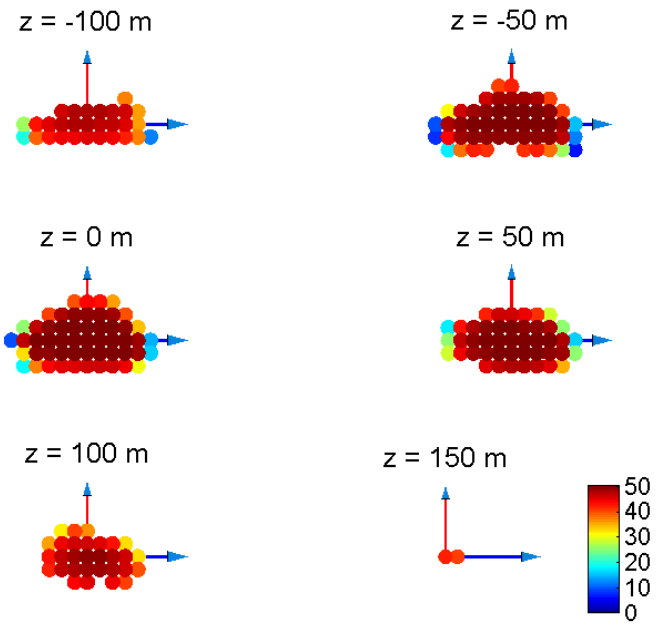

(b) Density uncertainties along the x-y plane (%).

Figure 7. *Case 1* trajectory based on 31.02 m finite-sphere radius.

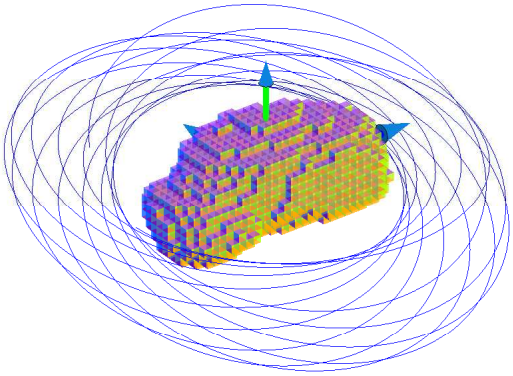

(a) 3-d trajectory and finite-cube shape model (3292 elements).

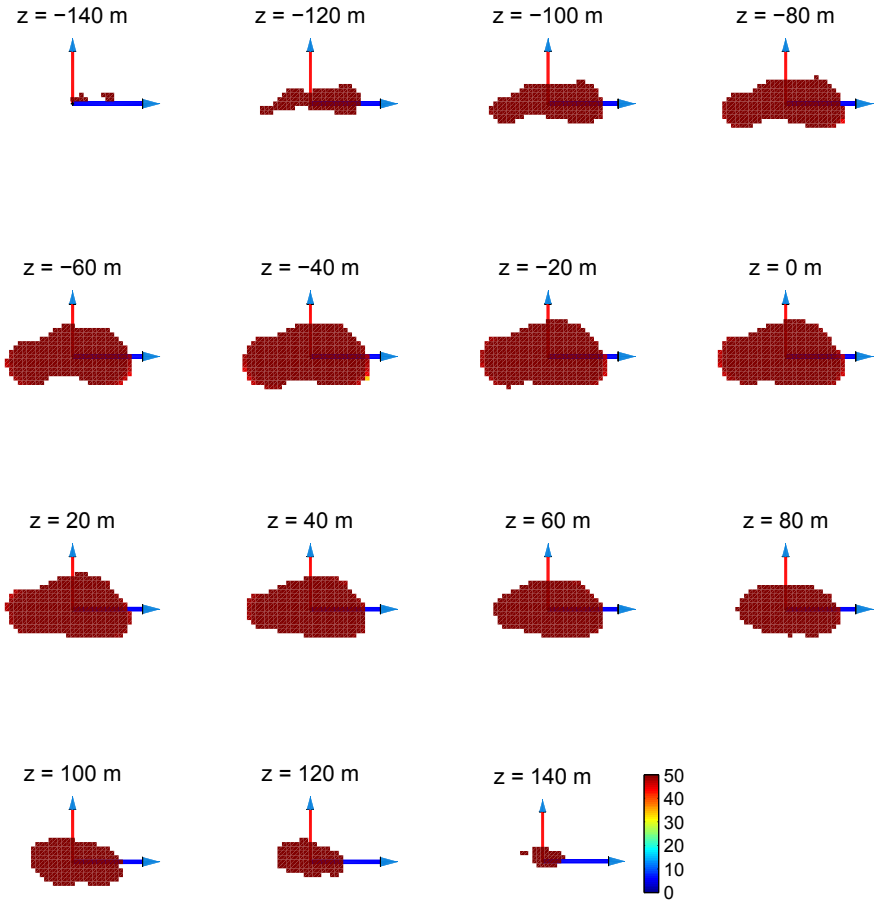

(b) Density uncertainties along the x-y plane (%).

Figure 8. *Case 1* trajectory based on 20 m cube resolution.

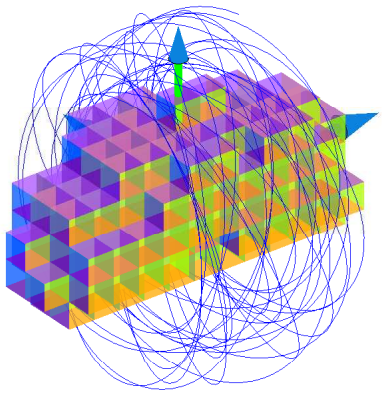

(a) 3-d trajectory and finite-cube shape model (211 elements).

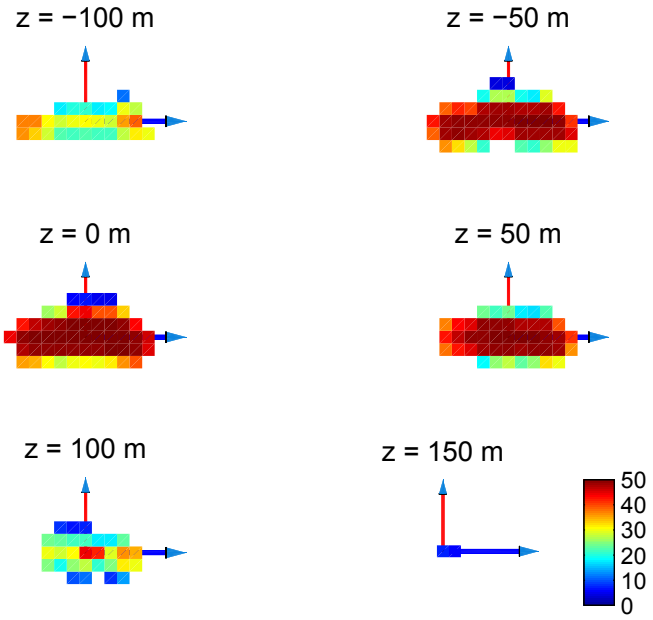

(b) Density uncertainties along the x-y plane (%).

Figure 9. *Case 2* trajectory based on 50 m cube resolution.

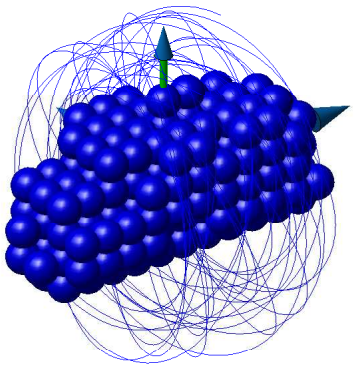

(a) 3-d trajectory and finite-sphere shape model (211 elements).

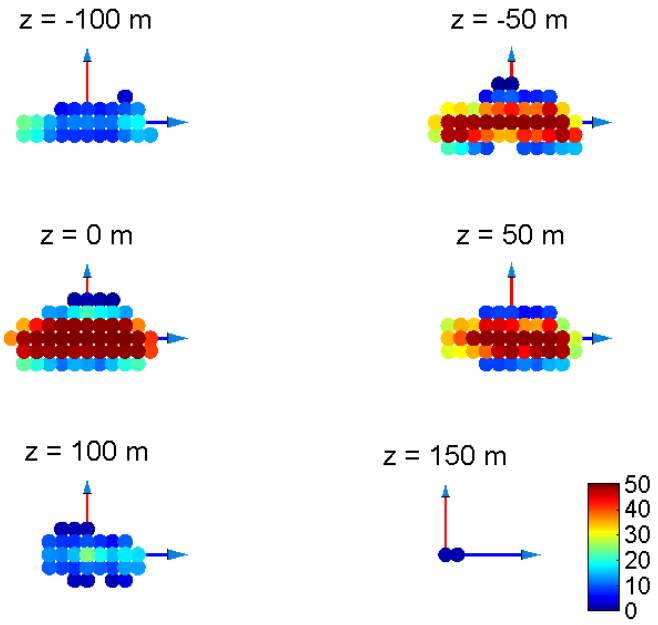

(b) Density uncertainties along the x-y plane (%).

Figure 10. ***Case 2*** **trajectory based on 30.02 finite-sphere radius assuming the measurement accuracy of 0.5 m and 0.0075 mm/s for range and range-rate data, respectively.**